



Polydopamine bridging strategy enables pseudomorphic transformation of multi-component MOFs into ultrasmall NiSe/WSe₂@NC heterojunctions for enhanced alkaline hydrogen evolution

Zhaodi Huang ^a, Shoufu Cao ^a, Chao Feng ^a, Youcong Li ^b, Yucang Liang ^c, Xunlu Li ^d, Hao Mei ^a, Weidong Fan ^a, Ben Xu ^a, Shuai Yuan ^{b,*}, Fangna Dai ^a, Xiaoqing Lu ^a, Songqing Hu ^a, Daofeng Sun ^{a,*}

^a State Key Laboratory of Heavy Oil Processing, School of Materials Science and Engineering, College of Chemistry and Chemical Engineering, China University of Petroleum (East China), Qingdao 266580, China

^b State Key Laboratory of Coordination Chemistry, Key Laboratory of Mesoscopic Chemistry of MOE, School of Chemistry and Chemical Engineering, Nanjing University, Nanjing, Jiangsu 210023, China

^c Institut für Anorganische Chemie, Eberhard Karls Universität Tübingen, Auf der Morgenstelle 18, 72076 Tübingen, Germany

^d Department of Materials Science, Fudan University, Shanghai 200433, China



ARTICLE INFO

Keywords:

Polydopamine bridging strategy
Multi-component MOFs
Pseudomorphic transformation
Ultrasmall heterojunctions
Alkaline hydrogen evolution

ABSTRACT

Heterojunction catalysts can synergistically promote the kinetics of energy-related reactions, but a significant challenge remains in fully exposing and engineering interfacial active sites. Herein, we developed a polydopamine (PDA) bridging strategy to construct multi-component metal-organic frameworks (MOFs) precursors to form ultrasmall NiSe/WSe₂@NC heterojunctions. Due to the ambiphilic binding of PDA to both NiMg-MOF and polyoxometalate (POM = H₃PW₁₂O₄₀), subsequent selenization and MgO removal yield highly dispersed NiSe/WSe₂@NC with intimate heterointerfaces. By adjusting Mg²⁺ and POM loadings in PDA-NiMg-MOF-POM, the Ni:W:C ratios in NiSe/WSe₂@NC were fine-tuned, resulting in an optimized catalyst with low overpotential and high stability (21 mV at 10 mA·cm⁻² for 60 h in 1.0 M KOH), rivaling the commercial 20% Pt/C (30 mV). X-ray absorption spectroscopy and density-functional theory calculations unveil that such “PDA bridging” strategy ensures highly exposed dual active centers and induced charge redistribution on heterointerface, resulting in accelerated water adsorption/dissociation and H₂ evolution kinetics.

1. Introduction

Alkaline water electrolysis represents an eco-friendly and sustainable method to convert and store hydrogen at a large scale [1,2]. However, the sluggish water-dissociation step in alkaline conditions (2–3 orders of magnitude slower than that in acid) results in high-energy consumption and hinders industrial commercialization [3]. Currently, Pt-group metals (PGMs) remain the state-of-the-art catalysts for driving hydrogen evolution reaction (HER) in alkaline conditions, but their high cost limits the large-scale application [4]. Therefore, exploring non-noble metal electrocatalysts to accelerate the reaction kinetics is in great demand.

Transition metal chalcogenides (TMCs) have attracted significant attention owing to their low price, good electrical conductivity, and high

tunability. [5] However, single-site TMCs may not satisfy the energetic requirement of multiple intermediates during alkaline HER [6]. Heterojunction catalysts with dual-active sites have shown unique advantages to improving alkaline HER activity by introducing additional water dissociation sites through interfacial engineering. Moreover, coupling two or more components with distinct energy states could stimulate a built-in electric field around the intimate heterointerface, which allows for fast charge transport and facilitated reaction kinetics [7–9]. For example, Dai et. al constructed MoS₂/NiPS₃ heterojunction, which delivered the alkaline HER overpotential of 112 mV at 10 mA cm⁻², much lower than the corresponding single component TMCs [10]. Despite the encouraging progress, it is still challenging to fully expose the interfacial active sites of heterojunction catalysts to further improve the HER performances. Accordingly, an effective strategy is to reduce

* Corresponding authors.

E-mail addresses: syuan@nju.edu.cn (S. Yuan), dfsun@upc.edu.cn (D. Sun).

the size of heterojunction nanoparticles to maximum atom utilization, and an average size between 2 and 5 nm will achieve both activity and stability [11,12]. Metal-organic frameworks (MOFs) represent a class of suitable precursors to avoid the aggregation of TMCs and expose the active heterojunction interfaces [13–15]. Taking advantage of the diverse chemistry of MOFs, heterometals can be introduced onto the inorganic nodes or into the cavity of MOFs. For example, polyoxometalates (POMs), inorganic molecular clusters with small sizes (1 nm) [16], have been incorporated into MOFs as metal resources for the synthesis of heterojunction catalysts [17,18]. However, the impregnated POMs from the traditional pore adsorption method usually interact weakly with the MOF cavity, leading to POM migration/leaching problems during thermal pyrolysis [19]. Meanwhile, without effective protective or isolating layers, the metal ions of MOFs tend to form aggregated particles (> 5 nm), which hinders the exposure of interfacial active sites [20].

Herein, we creatively proposed the “polydopamine (PDA) bridging” strategy to achieve the precise construction of ultrasmall heterojunction catalysts with an average diameter of 2.75 ± 1.5 nm. To realize this design, a well-defined mesoporous NiMg-MOF (3 nm, $[(\text{Ni}_x\text{Mg}_{1-x})_2\text{PDSA}]$, PDSA = pyromellitic diimide salicylic acid) was initially designed. Then, PDA and POM ($\text{H}_3\text{PW}_{12}\text{O}_{40}$) were successively incorporated into the mesopores of NiMg-MOF to fabricate the potent pre-assembling platform, denoted as $\text{PDA}\subset\text{NiMg-MOF-POM}$. Compared with traditional MOF-encapsulation strategy (Fig. 1A, Path I), our

strategy (Fig. 1A, Path II) utilizes PDA to electrostatic interaction MOFs with POMs, which restricts the migration of metal ions during pyrolysis. Meanwhile, partially replacing Ni^{2+} by Mg^{2+} in metal-oxo chains also helps to isolate Ni^{2+} and modulate the Ni:W:C ratio. On basis of this, subsequent selenization and MgO removal of $\text{PDA}\subset\text{NiMg-MOF-POM}$ precursor give rise to ultrasmall NiSe/WSe_2 heterojunctions embedded in N-doped carbons with intimate heterointerfaces. By adjusting the Ni, W, and C ratios in the precursors, the optimized $\text{NiSe}/\text{WSe}_2 @\text{NC}$ catalyst displays excellent alkaline HER performance with a low overpotential of 21 mV at $10 \text{ mA}\cdot\text{cm}^{-2}$ and outstanding stability (up to 60 h), rivaling that of 20% Pt/C. X-ray absorption spectroscopy (XAS) and density-functional theory (DFT) calculations suggest that coupling NiSe and WSe_2 with different work functions will induce a built-in electric field, leading to effective charge transfer and redistribution at the WSe_2/NiSe interface. The dual active centers of Ni and W along the heterointerface are endowed with an improved capability to cleave HO-H bonds and subsequently release H_2 , resulting in accelerated Volmer/Heyrovsky kinetics. When coupled with the $(\text{NiFe})\text{OOH}$ anode, the assembled $\text{NiSe}/\text{WSe}_2 @\text{NC} = |(\text{NiFe})\text{OOH}$ water electrolyzer only requires a low cell voltage of 1.55 V to drive the current density of $40 \text{ mA}\cdot\text{cm}^{-2}$, which is superior to that of $\text{Pt/C}||\text{RuO}_2$ electrolyzer (1.72 V at $40 \text{ mA}\cdot\text{cm}^{-2}$).

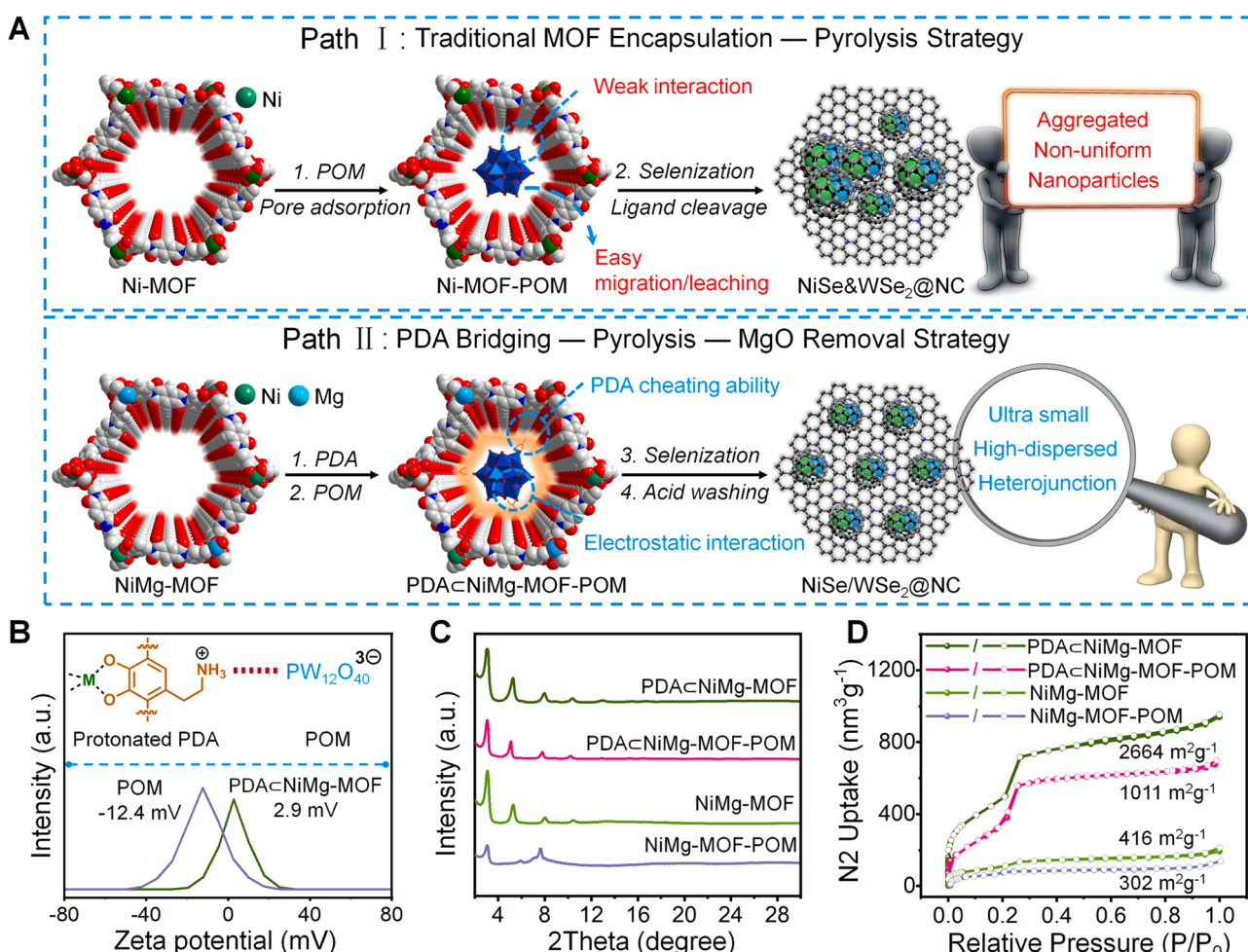


Fig. 1. (A) The comparison for the traditional MOF encapsulation-pyrolysis strategy (Pathway I), and PDA bridging-pyrolysis-MgO removal strategy (pathway II). Ni, Mg, C, N and O are represented by green, cyan, grey, blue, and red, respectively, and H atoms are omitted for clarity. (B) Schematic illustration of electrostatic interaction between protonated PDA and POM (top), and zeta potentials of POM and PDA \subset NiMg-MOF (bottom). (C) PXRD patterns, and (D) N_2 adsorption isotherms of PDA \subset NiMg-MOF, PDA \subset NiMg-MOF-POM, NiMg-MOF, and NiMg-MOF-POM.

2. Experimental section

2.1. Materials and reagents

All reagents and solvents were commercially available and used as received. 1,2,4,5-Benzenetetracarboxylic anhydride ($C_{10}H_2O_6$), 5-amino-2-hydroxybenzoic acid ($C_7H_7NO_3$), nickel nitrate hexahydrate ($(Ni(NO_3)_2 \cdot 6 H_2O$, 99%), magnesium nitrate hexahydrate ($(Mg(NO_3)_2 \cdot 6 H_2O$, 99%), and $H_3PW_{12}O_{40} \cdot xH_2O$ (POM) were provided by TCL Chemical. Dopamine HCl, dry sodium hydride 95% and anhydrous solvents were purchased from Sigma Aldrich and used without further purification. Anhydrous dimethylformamide (DMF), ethanol (EtOH), diethyl ether (Et₂O), methanol (MeOH), and hydrochloric acid (HCl) were all purchased from Sinopharm. Ultra-pure water was obtained by the Millipore Milli-Q water purification system (18.2 MΩ·cm, 25 °C).

2.2. Synthesis of free-base dopamine

In a N_2 purged, a 2-neck round bottom flask was charged with 2 g of dopamine HCl mixed in 20 mL of anhydrous tetrahydrofuran (THF) and 20 mL of anhydrous methanol. A total of 0.26 g of dry sodium hydride 95% was added slowly in small quantities over a period of approximately 25 min. The reaction mixture was allowed to stir for 40 h under flowing N_2 . After the completion of the reaction, the mixture was filtered under vacuum and washed with copious amounts of THF. The white powder was dried and kept under vacuum until further use.

2.3. Synthesis of ligand H_4PDSA

A dry 100 mL three-necked flask was added to a 1,2,4,5-benzenetetracarboxylic anhydride (9.97 g, 37.2 mmol), 5-amino-2-hydroxybenzoic acid (11.72 g, 76.5 mmol), and DMF (350 mL) solution with vigorously stirring for 10 min. The three-necked flask was then purged with N_2 until the air in the solution was completely removed. After that, it was heated at 130 °C for 24 h with continuous stirring. Finally, the mixture was filtered, washed three times with DMF, Et₂O, and MeOH in the proper sequence, and then dried in vacuum at 60 °C for 12 h to yield an orange powder. The final H_4PDSA was obtained by purifying the orange powder and soaking it with 2 M HCl (100 mL) for one day.

2.4. Synthesis of $PDA \subset NiMg\text{-}MOF\text{-}POM_x$ precursors

$Ni(NO_3)_2 \cdot 6 H_2O$ (52 mg), $Mg(NO_3)_2 \cdot 6 H_2O$ (50 mg), and H_4PDSA (100 mg) in a solvent mixture (DMF: EtOH: H_2O = 7.5 mL:0.5 mL:0.5 mL) were sonicated for 15 min, sealed in a 10 mL glass vial, and placed in an oven at 120 °C for 24 h. After cooling to room temperature, the obtained NiMg-MOF was washed three times with DMF and MeOH. Freshly made NiMg-MOF suspension in 30 mL MeOH was then placed in a 100 mL round-bottom flask and stirred for 5 min. Afterward, a solution containing PDA (10 mg) and 10 mL of MeOH was added to the round-bottom flask at room temperature. The sealed round-bottom flask was connected to the air with a needle. After stirring for 12 h, the product was washed twice with MeOH to obtain $PDA \subset NiMg\text{-}MOF$. Finally, $PDA \subset NiMg\text{-}MOF$ suspension in 30 mL MeOH was mixed with POM (30 mg) and stirred for 0, 2, 6, or 12 h at room temperature. The solid was separated by centrifugation and washed thoroughly with MeOH. The product was dried at 80 °C for 10 h in a vacuum to obtain $PDA \subset NiMg\text{-}MOF\text{-}POM_x$, where x indicates the weight percent of POM at different reaction times. The synthesis for $PDA \subset Ni\text{-}MOF\text{-}POM_x$ and $PDA \subset Mg\text{-}MOF\text{-}POM_x$ precursors follows a similar procedure using 104 mg of $Ni(NO_3)_2 \cdot 6 H_2O$ or $Mg(NO_3)_2 \cdot 6 H_2O$ as metal resources, respectively.

2.5. Synthesis of $NiSe/WSe_2 @NC$ heterojunctions

$PDA \subset NiMg\text{-}MOF\text{-}POM_x$ precursors (10 mg) and Se powder (20 mg)

were placed upstream and downstream in the porcelain boat of a tube furnace. The furnace was first heated to 400 °C for 2 h and then heated to 900 °C for 2 h at a ramping rate of 5 °C min⁻¹ under an Ar atmosphere. The product was immersed in 3.0 M HCl solution for 6 h for three times to remove MgO. The solid was washed with water and dried under 60 °C for 12 h to obtain $NiSe/WSe_2 @NC$ heterojunction catalysts. The preparation of $NiSe @NC$ and $WSe_2 @NC$ is similar to that of $NiSe/WSe_2 @NC$ except that the precursors for the reaction are $PDA \subset Ni\text{-}MOF\text{-}POM_0$ and $PDA \subset Mg\text{-}MOF\text{-}POM_{31.38}$.

2.6. Electrochemical characterization for HER in 1.0 M KOH

Electrochemical tests were carried out on a Gamry Reference 3000 electrochemical workstation at room temperature. All HER measurements were performed in 1.0 M KOH electrolyte, and the solution was purged with high-purity H_2 for at least 30 min before testing. The electrochemical testing was evaluated in a standard three-electrode setup with a glassy carbon electrode (GCE) as the working electrode (diameter: 3 mm; area: 0.07065 cm²), a carbon rod as the counter electrode (diameter: 3 mm) and saturated Ag/AgCl as the reference electrode. Generally, cyclic voltammograms (CVs) were carried out until a steady state was reached. Then, the linear sweep voltammetry (LSV) data were measured from 0 to -0.6 V at a scanning rate of 5 mV·s⁻¹. All the measured potentials were calibrated to the reversible hydrogen electrode (RHE) according to the equation ($E_{RHE} = E_{Ag/AgCl} + 1.02$). The LSV curves were plotted as overpotential vs. log current density and converted to Tafel plots. The electrochemical double layer capacitance (C_{dl}) was calculated from the CV curves measured at various scanning rates from 20 to 100 mV·s⁻¹. Electrochemical impedance spectroscopy (EIS) was performed in the frequency range from 100 kHz to 0.01 Hz by applying an AC amplitude of 10 mV. Afterward, the electrochemical stability was assessed by repeated cyclic voltammetry (CV) and chronoamperometric response curves at a fixed voltage with a scanning rate of 50 mV·s⁻¹.

2.7. Electrochemical measurements for overall water splitting in 1.0 M KOH

5 mg active samples were dispersed in a water/ethanol solution (500 μ L, 3:1 v/v) with 25 μ L of Nafion solution by sonication for 2 h to form a homogeneous ink. Then, 200 μ L of the uniform ink was drop-casted on carbon cloth (CC: 1.0 × 1.0 cm²) and dried at room temperature (mass loading: 1.0 mg·cm⁻²). A piece of CC was carefully pretreated by sonication in 6.0 M HCl, DI water, and ethanol for 15 min, respectively, to remove surface oxide. In this study, CC was chosen as the conductive substrate because it is porous and has a negligible catalytic or noncatalytic activity in the investigated potential region.

2.8. Calculation details

All calculations were carried out by spin-polarized density functional theory (DFT) as implemented in Vienna Ab initio Simulation Package (VASP) 6.1.1 with the Perdew-Burke-Ernzerhof (PBE) generalized gradient approximation (GGA). The cutoff energy was set as 420 eV after cutoff testing, and the k-points were set to 3 × 3 × 1 for geometry optimization. The electronic energy and forces converged to within 10⁻⁵ eV and 0.02 eV/Å, respectively. The van der Waals interactions were considered by the method of Grimme (DFT+D3). The effect of water was taken into consideration using the VASP implicit solvent model.

Changes in Gibbs free energy were calculated by the computational hydrogen electrode (CHE) model, in which the reaction $H^+(aq) + e^- = 1/2 H_2(g)$ is equilibrated at 0 V vs the reversible hydrogen electrode at all pH values. The change in Gibbs free energy (ΔG) for each elementary step was defined as follows. Changes in Gibbs free energy were calculated by the computational hydrogen electrode (CHE) model, in which the reaction $H^+(aq) + e^- = 1/2 H_2(g)$ is equilibrated at 0 V vs

the reversible hydrogen electrode at all pH values. The change in Gibbs free energy (ΔG) for each elementary step was defined as follows:

$$\Delta G = \Delta E + \Delta E_{ZPE} - T\Delta S + \Delta G_U + \Delta G_{pH}$$

where ΔE is the reaction energy, ΔE_{ZPE} and ΔS are the zero-point energy (ZPE) and the entropy difference between the products and the reactants at room temperature ($T = 298.15$ K), respectively. ΔG_U is the contribution of the applied electrode potential (U) to ΔG and is set as 0 V. ΔG_{pH} represents the free energy contribution due to the variations in H concentration, and the contribution of pH was excluded from consideration in this work.

3. Results and discussion

3.1. Design of multi-component MOF precursors

A mesoporous MOF with pyromellitic diimide moieties was initially designed as a matrix for the following reasons (Fig. S1). First, the mesoporous framework structure provides enough pore space for the post-synthetic incorporation of PDA and POM. Second, the coordinatively unsaturated metal sites of MOFs may bind with the phenolic hydroxyl groups from PDA, while the electron-deficient pyromellitic diimide moiety on the MOF linkers will interact with electron-rich dopamine to favor the adsorption of dopamine monomers and subsequent formation of PDA in the pore. Third, the concentration of Ni in the MOF precursor can be diluted by forming bimetallic NiMg-MOFs where inert Mg species can be removed after selenization. As expected, the reaction of H₄PDSA, Ni(NO₃)₂·6 H₂O and/or Mg(NO₃)₂·6 H₂O in DMF/ethanol/water at 120 °C gave rise to isostructural Ni-MOF, NiMg-MOF, and Mg-MOF microcrystalline powders.

The structures of Ni-MOF, NiMg-MOF, and Mg-MOF were confirmed by powder X-ray diffraction (PXRD) analysis combined with structural simulations using Materials Studio. As shown in Figs. S2 A-C and Table S1, pawley refinements of PXRD patterns based on an $R\bar{3}3$ space group give similar lattice parameters ($a = b = 59.8119$ Å, $c = 6.7063$ Å, for Ni-MOF; $a = b = 59.6929$ Å, $c = 6.6588$ Å, for NiMg-MOF, $a = b = 59.8831$ Å, $c = 6.7400$ Å, for Mg-MOF). The three MOFs all exhibit a MOF-74-type structure, which is composed of metal-oxo chains bridged by PDSA forming hexagonal channels. The pore size is estimated to be ~3.0 nm based on the structural model, which is similar to several previous MOF-74 analogs [21,22]. Note that NiMg-MOF has a PXRD pattern similar to those of Ni- and Mg-based analogs, which all match well with the simulation based on the structural models (Fig. S2D). The diffraction peaks at 2.95°, 5.11°, and 7.82° can be attributed to the (120), (030), and (450) facets, respectively. As displayed in Figs. S3A-C, the scanning electron microscopy (SEM) image reveals a chestnut-like NiMg-MOF nanoparticle composed of needle-shaped nanorods, which is similar to the Ni-MOF and Mg-MOF. The SEM-EDX elemental mappings further indicate the uniform distribution of Ni²⁺ and Mg²⁺ ions in NiMg-MOF particles (Fig. S3D). The inductively coupled plasma (ICP) analysis for NiMg-MOF indicates a Ni/Mg molar ratio of 1.96 (Table S2), corresponding to a formula of Ni_{0.66}Mg_{0.33}PDSA. Therefore, the Ni-, NiMg-, and Mg-MOF series can be formulated as (Ni_xMg_{1-x})₂PDSA ($x = 0, 0.66$, and 1).

3.2. Effect of PDA on stabilizing MOFs and adsorbing POMs

Dopamine (DA) monomers were adsorbed into the MOF cavity and spontaneously polymerized to form PDA (Figs. S4). The loading of PDA was determined to be 10.86 wt% based on TGA (Figs. S5), which is consistent with the ICP—OES result (9.45 wt%, Fig. S6). Subsequently, a Keggin-type POM (H₃PW₁₂O₄₀) with a molecular size of 13 Å was selected as a W resource and readily diffuses into the mesopores of PDACNiMg-MOF. The adsorption of POMs was carried out by incubating NiMg-MOF in a methanol solution of H₃PW₁₂O₄₀ at room temperature.

The loading of POMs in PDACNiMg-MOF-POM was monitored by UV-vis spectroscopy. As shown in Fig. S7, PDA-modified MOFs (PDACNi-MOF, PDACNiMg-MOF, and PDACMg-MOF) show comparably high POM uptakes (~30 wt%), which are much higher than the NiMg-MOF without PDA (~1 wt%). Meanwhile, the FT-IR spectra of PDACNiMg-MOF-POM exhibited four new peaks at 791 cm⁻¹, 824 cm⁻¹, 951 cm⁻¹ and 1063 cm⁻¹. They are attributed to W-Ob-W, W-O_c-W, W=O_d, and P-O_e of POM, respectively, verifying the successful encapsulation of POM into PDACNiMg-MOF framework (Fig. S8). However, NiMg-MOF-POM without PDA has no apparent absorption in this region. We propose that the residual amino groups (-NH₂) on PDA act as anchor sites to adsorb POM through electrostatic interactions [23]. This hypothesis is supported by zeta potential measurements, in which PDACNiMg-MOF possesses a positive surface charge (2.9 mV) and POM has a negative charge (-12.4 mV) (Fig. 1B). XPS further confirmed the partial transformation of -NH₂ species (PDACNiMg-MOF) into -NH₃⁺ (PDACNiMg-MOF-POM), corresponding to the protonation of -NH₂ groups by H₃PW₁₂O₄₀ to form -NH₃⁺/[PW₁₂O₄₀]³⁻ pairs (Fig. S9).

PDA is important for the subsequent loading of POM because it stabilizes the NiMg-MOF from collapse and enhances the absorption of POM. The NiMg-MOF collapses upon direct activation under vacuum at 150 °C, while PDA in PDACNiMg-MOF helps to prevent framework collapse. As shown in Fig. 1C, PDACNiMg-MOF maintained their crystallinity porous structure after POM loading. For comparison, the PXRD peak intensity of NiMg-MOF-POM without PDA degrades after incubating in POM solutions for 12 h, possibly due to the acidity of H₃PW₁₂O₄₀ and the competitive coordination of [PW₁₂O₄₀]³⁻ anions with metal cations in NiMg-MOF. The stability enhancement of NiMg-MOF by PDA can be further confirmed by N₂ adsorption/desorption curves (Fig. 1D and S10). While PDACNiMg-MOF largely maintained its porosity and Brunauer–Emmett–Teller (BET) surface area after POM adsorption, NiMg-MOF without PDA showed a significantly reduced BET surface area, suggesting pore collapse. Note that the pore size of NiMg-MOF is estimated to be 3.0 nm based on the crystal structure, however, it is difficult to experimentally measure the pore size of NiMg-MOF by N₂ adsorption because it collapses upon activation. Similar stability enhancement has been documented in other polymer-loaded MOFs, where the polymers prevent the coordination bonds from being attacked by guest molecules [24,25]. In addition, the polymers were also reported to immobilize the organic linkers and reduce the torque on the metal-ligand coordination bonds to enhance mechanical stability [21, 26]. Meanwhile, PDA and POM incorporation did not change the particle size, morphology, or uniform elemental distributions of the materials, as confirmed by SEM and EDX elemental mappings (Figs. S11–14).

In addition to the high porosity and uniformly distributed Ni/W/C elements, the ratios of Ni/W/C elements in the precursors are also important for the electrocatalytic properties of the derived NiSe/WSe₂ @NC nanomaterials. The ratio between Ni, W, and C elements was tuned by adjusting the Ni ratio from 19.83 to 11.15 wt% in the mixed-metal MOFs and varying the POM loading from 0 to 31.88 wt%. The W content was controlled by incubating MOFs in POM solutions for 0, 2, 6, and 12 h, giving rise to PDACMOF-POM_x, where x indicates the weight percent of POM (Fig. S15). Taking the PDACNi-MOF-POM_x series as an example, the loading of POM was estimated to be 0, 25.44 wt%, 30.45 wt%, and 33.31 wt% by UV-vis after 0, 2, 6, and 12 h (Table S2). The saturated POM uptake (33.31 wt% based on UV-vis) matched well with the ICP-OES (28.69 wt%), TGA (31.1 wt%), and EDX (25.98 wt%) results (Table S3, and Figs. S16 and S17). Using multi-component MOF precursors with different Ni/W/C ratios, we expect to obtain a series of NiSe/WSe₂ @NC materials with variable Ni/W/C ratios.

3.3. Synthesis and characterization of NiSe/WSe₂ @NC heterojunctions

The NiSe/WSe₂ @NC heterojunctions were synthesized by pyrolysis of PDACNiMg-MOF-POM precursors with Se powder and the MgO impurity was subsequently removed by acid washing (Fig. S18). All the

samples show characteristic diffraction peaks of NiSe (PDF#75–0610, highlighted in blue) and WSe₂ (PDF#87–2418, highlighted in green), except for PDACNi-MOF and PDACMg-MOF, which only show NiSe or carbon phases due to the lack of POMs (Fig. S19). The relative intensities of NiSe and WSe₂ diffraction peaks vary in these samples, corresponding to the different Ni/W ratios. Taking the PDACNiMg-MOF-POM derivative as an example, the SEM images in Fig. 2A and B indicate that NiSe/WSe₂ @NC inherits the chestnut-like morphology from the precursor. The sizes of spherical particles (diameter: $\sim 2 \mu\text{m}$) and needle-shaped nanorods ($\sim 75 \text{ nm} \times 220 \text{ nm}$) are similar to the NiMg-MOF precursors (Fig. S20). However, the TEM image shows that ultrafine nanoparticles are uniformly embedded in the nanorods (Fig. 2C). The mean diameter of the nanoparticles is approximately $2.75 \pm 1.5 \text{ nm}$ (Fig. 2D and inset of Fig. 2C). The highly dispersed nanoparticles can maximize atomic utilization and realize a high exposure of active sites, which helps to improve the accessible surface area [27]. The high-resolution TEM (HRTEM) image of Fig. 2E reveals two sets of different lattice spacings, with a red dashed line highlighting the intimate heterointerface. The lattice spacings of 0.272 and 0.65 nm are indexed to the (101) and (002) planes of NiSe and WSe₂, respectively. This observation is consistent with the lattice spacings obtained from the

line scan of the corresponding area in the HRTEM image (Fig. 2F). A series of concentric rings can be observed in the selected area electron diffraction (SAED) image, corresponding to the polycrystalline NiSe and WSe₂ phases (Fig. 2G). Furthermore, the elemental mappings illustrate the uniform distribution of Se, Ni, W, C, and N on the NiSe/WSe₂ @NC heterojunctions (Fig. 2H). Combining the results of ICP-OES and EDS, the Ni, W and Se contents of are calculated to be 17.39 wt.%, 17.31 wt.%, and 42.64 wt.%, respectively (Table S2 and Fig. S21). In addition, the Brunauer-Emmett-Teller (BET) specific surface area of NiSe/WSe₂ @NC is $220.52 \text{ m}^2 \cdot \text{g}^{-1}$, and the pore sizes are mainly distributed in the micro- and mesopore range (1.7–2.8 nm) (Fig. S22). The high specific surface area and micro/mesoporous structure can largely facilitate the mass diffusion of reactants, thus benefiting their electrocatalytic activity [28]. It should be noted that PDA is critical for the pseudomorphic transformation of PDACNiMg-MOF-POM precursors into small and uniform NiSe/WSe₂ nanoparticles. Control experiments were also conducted by using NiMg-MOF-POM without PDA as precursors, which resulted in an irregular morphology with aggregated NiSe particles ($\sim 100 \text{ nm}$) (Figs. S23 and S24). The XRD peaks of its derivative mainly attributes to NiSe (PDF#75–0610), and only a few peaks indexing to WSe₂ (PDF#87–2418) can be seen but with low intensity, which are in well

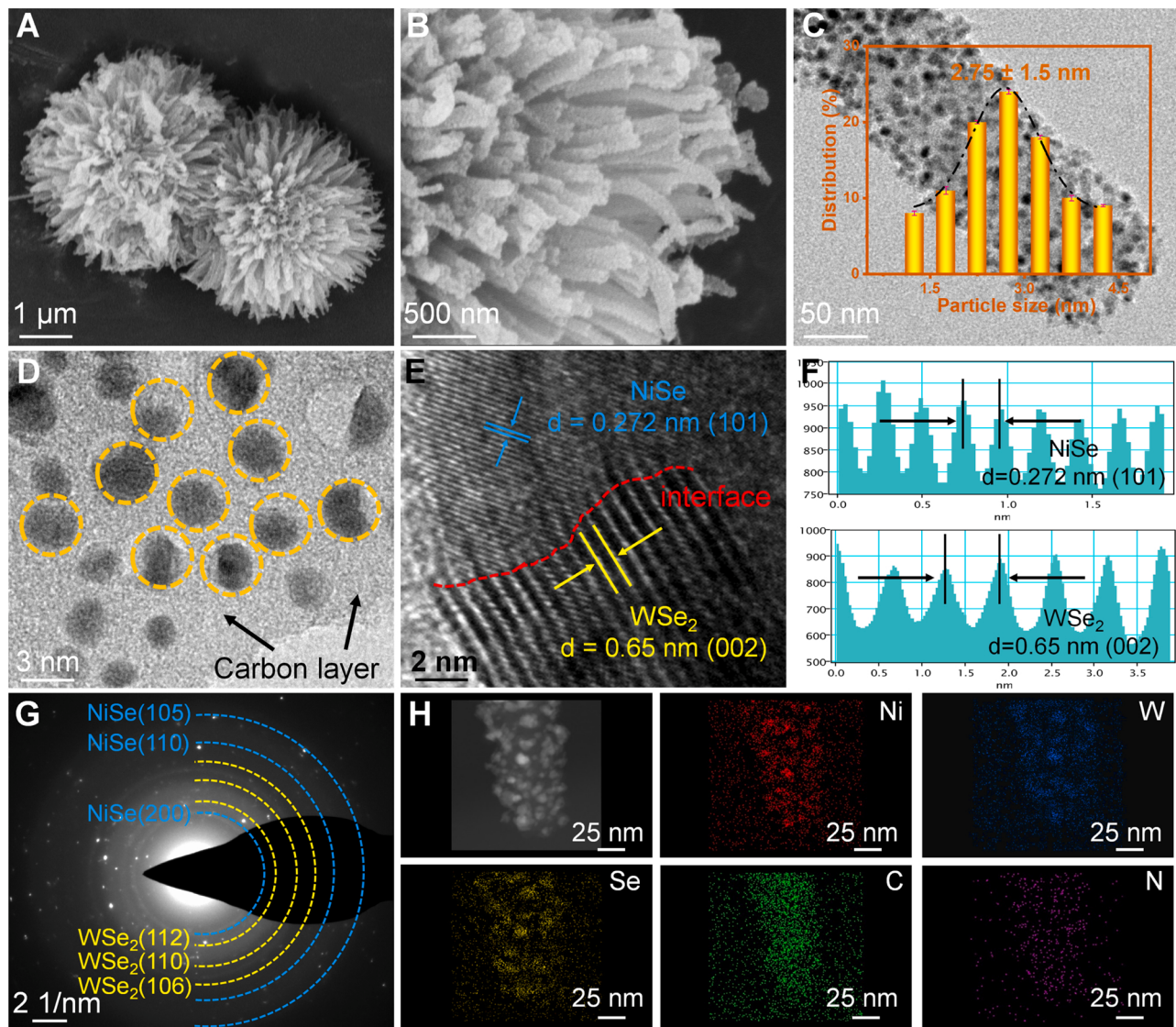


Fig. 2. (A and B) SEM images of NiSe/WSe₂ @NC heterojunctions. (C and D) TEM images (Inset of Fig. 2C shows particle size distribution) of NiSe/WSe₂ @NC heterojunctions. (E) HRTEM image of NiSe/WSe₂ @NC heterojunctions. (F) Profile plots of the calibration for measuring the spacing in panels of NiSe/WSe₂ @NC heterojunctions. (G) SAED pattern of NiSe/WSe₂ @NC heterojunctions. (H) HAADF image and STEM-EDS elemental mappings of NiSe/WSe₂ @NC heterojunctions.

accord with SEM and TEM observations (Fig. S25).

3.4. Optimization of HER catalytic activity

NiSe/WSe₂ @NC heterojunction electrocatalysts were tested in H₂-saturated 1.0 M KOH electrolyte with a standard three-electrode setup to evaluate its alkaline HER performance. IR-corrected linear sweep voltammetry (LSV) curves of NiSe/WSe₂ @NC with various Ni and W contents are compared in Fig. 3A. Generally, increasing POM loading (W content) enhances the HER activity of NiSe/WSe₂ @NC, as evidenced by the lower overpotentials at the same current density. Meanwhile, the Ni content also affects the HER current. The specific Ni and W contents are given in Table S3. The effect of Ni and W contents on the HER overpotential at the current density of 10 mA·cm⁻² (η_{10}) is shown in a contour plot (Fig. 3B). This trend indicates that a proper Ni/W/C ratio is necessary to maximize the active NiSe/WSe₂ interfaces and the HER activity. The optimal HER activity is achieved at a W content of 17.31 wt % and a Ni content of 17.39 wt%, which has an overpotential of 21 mV at 10 mA·cm⁻². The performance of NiSe/WSe₂ @NC even surpasses that of benchmark Pt/C catalysts with an overpotential of 30 mV at the same current density. The single component NiSe@NC and WSe₂ @NC

possess inferior HER activity with large overpotentials of 272 mV and 208 mV at 10 mA·cm⁻², respectively. Such enhanced HER activity of NiSe/WSe₂ heterojunction could be ascribed to high-dispersed active centers and intimate NiSe/WSe₂ heterointerfaces. The Tafel slopes provided were further analyzed to compare alkaline HER kinetics and reveal reaction mechanisms (Fig. 3C). Compared with NiSe@NC (118.7 mV·dec⁻¹), WSe₂ @NC (122.9 mV·dec⁻¹) and Pt/C (63.5 mV·dec⁻¹), the optimized NiSe/WSe₂ @NC shows a relatively small Tafel slope of 45.2 mV·dec⁻¹, indicating its favorable HER kinetics and Heyrovsky controlled mechanism. Such performance including the overpotentials (η_{10}) and Tafel slopes is the best of recently reported MOF- and POM-derived electrocatalysts (Tables S4 and S5), and also ranks among the best of heterojunction-based HER electrocatalysts (Fig. 3D).

Furthermore, cyclic voltammetry (CV) curves at different scan rates varying from 20 to 100 mV s⁻¹ were measured within a potential window from 0.175 to 0.275 V. They are further used to estimate the electrochemical double-layer capacitance (C_{dl}) and the electrochemical active surface area (ECSA), while the C_{dl} are proportional to the ECSA (Fig. S26). As shown in Fig. S27, the C_{dl} of NiSe/WSe₂ @NC (25.71 mF·cm⁻²) is larger than that of Pt/C (20.62 mF·cm⁻²), corresponding to

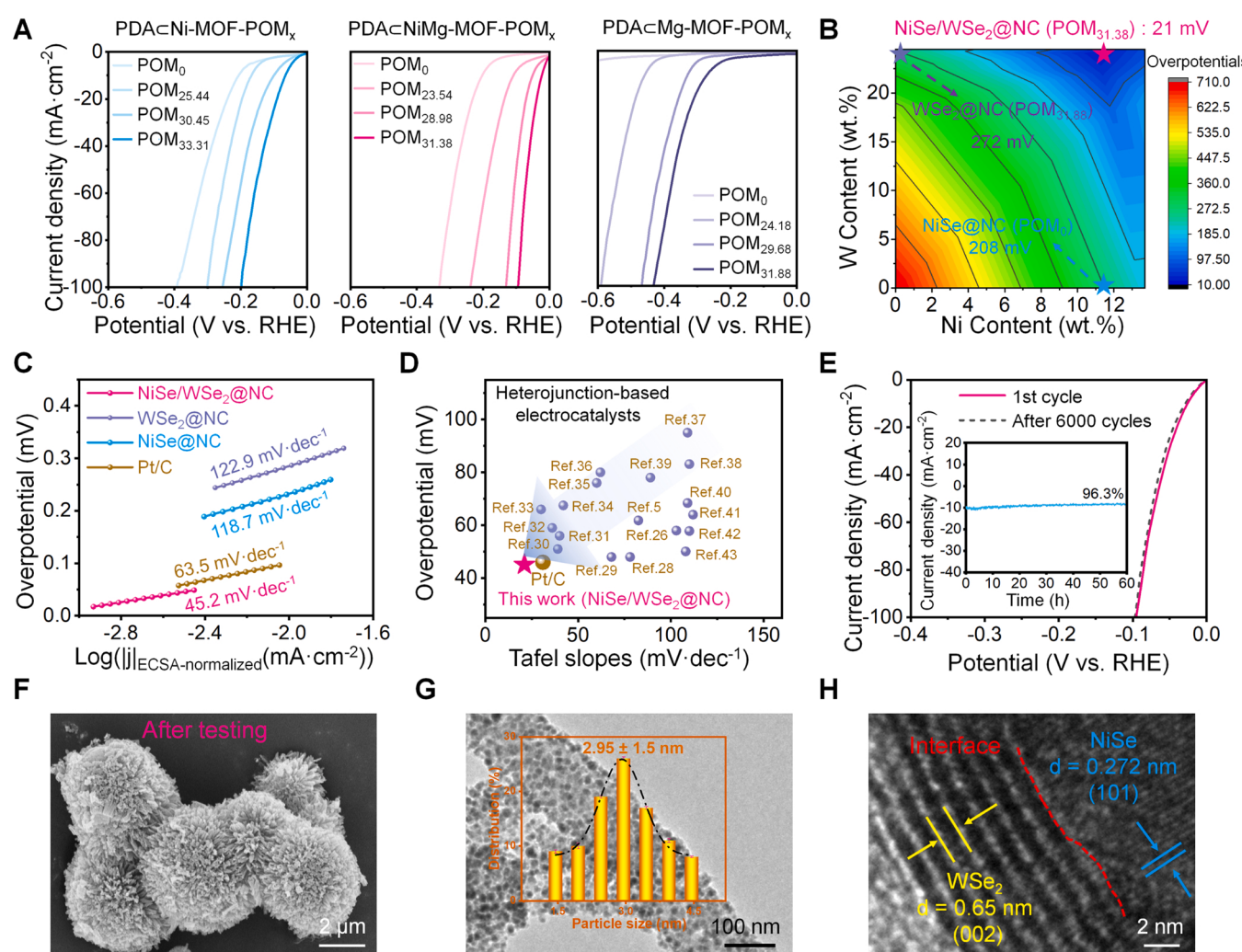


Fig. 3. (A) The LSV curves of NiSe/WSe₂ @NC, WSe₂ @NC, and NiSe@NC heterojunction catalysts derived from PDAcNi-MOF-POM_x, PDAcNiMg-MOF-POM_x, and PDAcMg-MOF-POM_x with different POM loadings. (B) Contour map of the overpotentials at current densities of 10 mA·cm⁻² against the Ni and W contents. (C) The Tafel slopes with current density normalized by the ECSA of NiSe/WSe₂ @NC, WSe₂ @NC, NiSe@NC, and Pt/C. (D) The comparison of alkaline HER performances for NiSe/WSe₂ @NC with recently reported heterojunction-based electrocatalysts in refs [29–44]. (E) The polarization curves before and after 6000 cycles of NiSe/WSe₂ @NC, with the inset showing the current density versus time (i-t) curve at a fixed potential of 21 mV. (F) The SEM, (G) TEM image, and (H) HRTEM images of NiSe/WSe₂ @NC after the long-term test.

the ECSA values of 642.75 and 589.14 cm², respectively. The large ECSA of NiSe/WSe₂ @NC can be attributed to the ultrasmall and tunable heterostructures, which can supply accessible surface active sites, benefit mass transport and subsequent charge transfer during the HER catalysis. To better compare the intrinsic HER activity, we further normalized the HER current by the electrochemical surface area (ECSA) of catalysts (Fig. S28). As shown, ECSA-normalized LSV curves indicate that NiSe/WSe₂ @NC heterojunctions still exhibited higher ECSA current and lower overpotential to drive the HER reaction. Electrochemical impedance spectra (EIS) and the associated Nyquist plots of all catalysts show typical semicircle profiles, which were fitted based on a simplified Randle circuit model (Fig. S29). The charge-transfer resistance (R_{ct}) for the top-performing NiSe/WSe₂/NC is 12.5 Ω, implying fast interfacial charge transfer rates during the HER. Moreover, NiSe/WSe₂ @NC not only shows barely changed LSV curves relative to the initial LSV curve of 2000 CV cycles, but also sustains 96.3% current density over 60 h of continuous i-t testing (Fig. 3E) [29–43].

Encouraged by the high HER activity and stability of NiSe/WSe₂ @NC, a water electrolyzer was assembled by coupling the NiSe/WSe₂ @NC cathode with the (NiFe)OOH anode in 1.0 M KOH electrolyte (Fig. S30) [44]. As presented in Fig. S31, the NiSe/WSe₂ @NC = |(NiFe)OOH electrolyzer only requires a low cell voltage of 1.55 V to achieve a current density of 40 mA·cm⁻². The NiSe/WSe₂ @NC = |(NiFe)OOH electrolyzer can also achieve a large current density of 160 mA·cm⁻² at 1.67 V. This performance is much superior to the Pt/C||RuO₂ coupled electrolyzer (1.72 V @ 40 mA·cm⁻²), and is among the highest in the literature (Table S6). The amount of O₂ and H₂ generated by NiSe/WSe₂ @NC heterojunctions at j_{50} is approximately 10.36 and 20.5 mL, corresponding to a nearly 98.11% and 99.2% faradaic efficiency for the alkaline HER (Fig. S32). Meanwhile, the NiSe/WSe₂ @NC = |(NiFe)OOH electrolyzer could drive water splitting using a commercially available 1.5 V single-cell AA battery, and numerous bubbles on the surface of the electrodes could be observed (Fig. S33). Continuous generation of H₂ and O₂ bubbles further illustrates that the NiSe/WSe₂ @NC = |(NiFe)OOH electrolyzer can realize overall water splitting at a low voltage steadily. Furthermore, the continuous cyclic voltammetry (CV) and chronopotentiometry tests were carried out to assess the stability of NiSe/WSe₂ @NC = |(NiFe)OOH electrolyzer. A current retention of 98.86% can be observed over a period of 40 h continuous i-t testing at 40 mA cm⁻². The polarization curves after 6000 cycles CV tests almost overlaps with the initial one, indicating excellent stability (Fig. S34). In addition, no obvious changes were observed in chestnut-like morphology, particle sizes, and heterointerface structures of NiSe/WSe₂ @NC after this stability testing, as evidenced by SEM, TEM, and HRTEM (Fig. 3F-H). The stability can be attributed to the micro-porous carbon support, which protects NiSe/WSe₂ nanoparticles from corrosion and aggregation. Meanwhile, the chemical state and elemental composition of NiSe/WSe₂ @NC after the durability test were also investigated (Fig. S35). It was found that all spectra of NiSe/WSe₂ @NC before and after the durability test showed the same fitted peaks, indicating its excellent stability toward overall water splitting. Note that most of the Ni species were transformed from the +2 to +3 valence, as evidenced by a distinct decrease in the Ni²⁺/Ni³⁺ atomic ratio of the Ni 2p_{3/2} and 2p_{1/2} peaks. This phenomenon is due to the occurrence of surface reconstruction during the OER process, which is in good agreement with the results previously reported in the literature [45]. Overall, the high activity and stability of NiSe/WSe₂ @NC demonstrate its great potential for practical applications.

3.5. Mechanistic study of NiSe/WSe₂ @NC heterojunctions

X-ray photoelectron spectroscopy (XPS) and X-ray and absorption spectroscopy (XAS) were adopted to investigate the electron structure and coordination environment of metal centers in NiSe/WSe₂ @NC. In the W 4f XPS spectrum of NiSe/WSe₂ @NC, two strong peaks at 32.8 and 34.9 eV are assigned to W⁴⁺ 4f_{7/2} and W⁴⁺ 4f_{5/2}, while the weak

broad bands centered at 37.8 eV originate from W⁶⁺ species from surface oxidation (Fig. 4 A). Compared to WSe₂, the W 4f peaks of NiSe/WSe₂ @NC are downshifted by ~0.24 eV. On the other hand, the high-resolution XPS spectrum of Ni 2p can be deconvoluted into some sub-peaks. Two peaks at 853.5 eV and 870.7 eV are identified as Ni 2p_{3/2} and Ni 2p_{1/2} of Ni-Se bond, and another two peaks at 855.6 and 874.5 eV can be ascribed to Ni 2p_{3/2} and Ni 2p_{1/2} of Ni-O bond [46–48]. The Ni-Se peaks were ~0.22 eV positively shifted in comparison to those of NiSe. The opposite peak shift direction of Ni and W indicates electron transfer from NiSe to WSe₂ [49]. This point could be further confirmed by XAS spectra. As shown in Fig. 4C, the whiteline peak intensity and absorption edge of NiSe/WSe₂ @NC in the W L₃-edge X-ray absorption near-edge structure (XANES) spectrum all downshifted. The result suggests that the formation of NiSe/WSe₂ heterostructure causes the increased electron density, and the valence state of W species is lower than +4 (inset of Fig. 4C). The W L₃-edge extended X-ray absorption fine structure (EXAFS) spectrum of NiSe/WSe₂ @NC shows two peaks at ~2.25 Å and ~3.4 Å, which are assigned to W-Se and W-W scattering feature (Fig. 4D) [50]. Compared with WSe₂, the decreased peak intensity of NiSe/WSe₂ @NC should be attributed to the interfacial atomic rearrangement caused by abundant heterointerfaces. Meanwhile, the Se K-edge adsorption edge positions of NiSe/WSe₂ @NC are comparable to WSe₂ and NiSe, implying the same valency of Se atoms (Fig. 4E). The slight difference reflected in zoom-in picture can be tentatively attributed to the different electron inductive effect of W and Ni (inset of Fig. 4E). As observed in the Se K-edge EXAFS analyses in Fig. 4F, a dominant peak at ~2.24 Å is between that of Ni-Se bond (2.05 Å) and W-Se bond (2.46 Å), which implies the coexistence of Ni-Se and W-Se bonds in the NiSe/WSe₂ @NC. Relative to W-Se bond, the radial distance of Ni(W)-Se is closer to that of Ni-Se bond due to the higher content of NiSe than WSe₂ in the NiSe/WSe₂ @NC. Another peak at 3.05 Å can be ascribed to Se-Se bond. The decreased peak intensity in comparison with NiSe and WSe₂ results from a relatively lower W content in the NiSe/WSe₂ heterojunction than in pure WSe₂ [51]. In addition, the results can also be confirmed by comparing the wavelet transform (WT) plots and corresponding R-space FT-EXAFS spectra (Fig. 4G-I and S35). Therefore, the lower oxidation state of W in NiSe/WSe₂ @NC than in WSe₂ indicates charge redistribution on the NiSe/WSe₂ heterojunction, in which NiSe donates electrons to WSe₂ to reduce the W oxidation state. The electron density redistribution on the NiSe/WSe₂ interface can alter the adsorption free energies toward H₂O species and H intermediates to affect the HER kinetics.

The work functions were first analyzed to verify the interfacial electron redistribution at the NiSe/WSe₂ interface by density functional theory (DFT) calculations. As shown in Fig. 5A, the work function of WSe₂ was calculated to be 5.67 eV, which is higher than that of NiSe (4.84 eV). Therefore, the contact potential at the NiSe/WSe₂ interface will induce a built-in electric field, resulting in electron transfer from NiSe to WSe₂ (Fig. 5B). Moreover, the charge density difference image show that the electrons of 1.83 e⁻ transfer from NiSe to WSe₂, resulting in the electron accumulation on WSe₂ and electron depletion on NiSe (Fig. 5C). The electron accumulation on WSe₂ favors the water dissociation energies, whereas the electron depletion on NiSe is beneficial for the release of H₂, thereby synergistically promoting alkaline HER activity. The d-band density of states (d-DOS) near the Fermi level was further analyzed to investigate the electronic structure difference of NiSe, WSe₂, and NiSe/WSe₂ (Fig. 5D). Based on the literature, the d-band center (E_d) relative to the Fermi level describes the adsorption energy of substrates on the metal center, where a downshift of E_d usually indicates the increased binding of O species and decreased adsorption of H species. The E_d of NiSe/WSe₂ is downshifted (away from the Fermi level) compared to NiSe and WSe₂, indicating stronger H₂O binding and weaker H-binding [52]. As expected, NiSe/WSe₂ presents a suitable water adsorption energy ($\Delta E(H_2O)$) of -1.07 eV at W sites and a Gibbs free energy of H^{*} (ΔG_{H^*}) of 0.37 eV at Ni sites, which are superior to those of NiSe and WSe₂ (Fig. 5E and F).

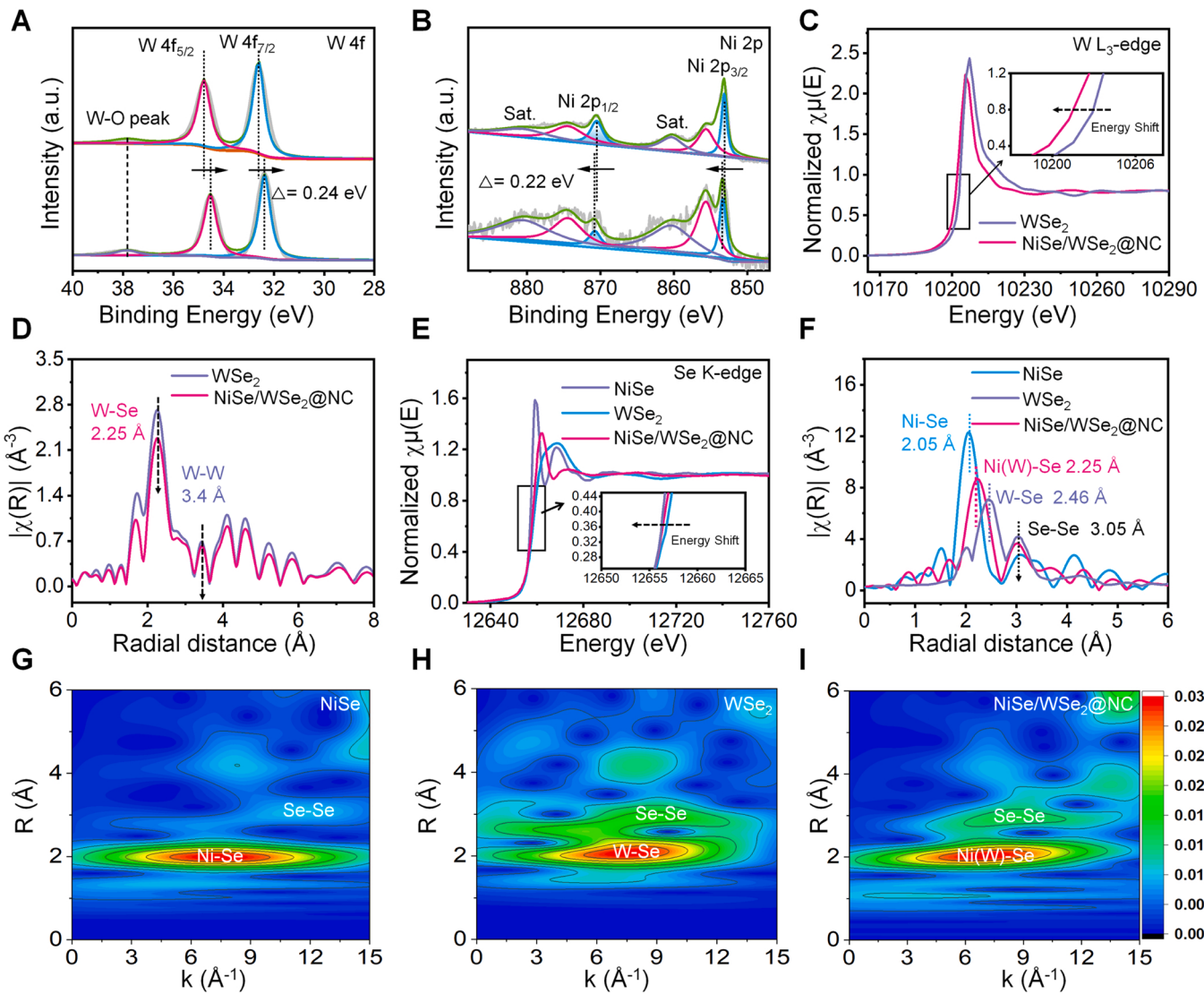


Fig. 4. (A) The XPS spectra of W 4f for WSe₂ (top) and NiSe/WSe₂ @NC (bottom). (B) The XPS spectra of Ni 2p for NiSe (top) and NiSe/WSe₂ @NC (bottom). (C) The W L₃-edge XANES of WSe₂ and NiSe/WSe₂ @NC. (D) The Fourier transformed EXAFS of WSe₂ and NiSe/WSe₂ @NC in R space. (E) The Se K-edge XANES, (F) the Fourier transformed EXAFS in R space, and (G, H, and I) the WT plots of the Se K-edge of NiSe, WSe₂, and NiSe/WSe₂ @NC, respectively.

We further proposed alkaline HER pathways to visualize the detailed energy parameters of intermediates on WSe₂, NiSe, and WSe₂/NiSe heterojunctions (Table S7). Generally, the alkaline HER pathways of NiSe/WSe₂ proceed through two steps, i.e., the water dissociation steps to form H* intermediates (Volmer step) and the evolution of H₂ (Heyrovsky step). As depicted in Fig. 5G, WSe₂ benefits the Volmer step with an energy barrier down to 0.17 eV, while NiSe is energetically favorable for the Heyrovsky step with an energy barrier of 0.18 eV. Integrating the two active centers into NiSe/WSe₂ significantly reduces the energy barrier for both Volmer and Heyrovsky steps. In particular, the water dissociation energy barrier for breaking the H-OH bond was slightly decreased to 0.04 eV when we chose interfacial W atoms as reaction sites. Combining the favorable water adsorption/dissociation and enlarged H-O bond length (Fig. 5H), we conclude that the H₂O molecules are first captured by W sites to weaken the H-O bond. Next, the H* intermediates are transferred to an adjacent interfacial Ni site to undergo subsequent H₂ formation. Thus, we conclude that the WSe₂/NiSe heterojunction has the optimal reaction energies for water dissociation and hydrogen evolution, thus boosting HER activity in alkaline media (Fig. 5I).

4. Conclusion

In conclusion, the PDA bridging strategy has been developed to obtain highly dispersed NiSe/WSe₂ heterojunctions anchored on N-doped carbons using multi-component MOF composites as precursors. By integrating MOF and POM through the PDA connecting bridge, the migration of metal species is restricted during the pyrolysis. As a result, pseudomorphic transformation of MOF precursors into NiSe/WSe₂ @NC has been realized, ensuring highly dispersed NiSe/WSe₂ interfacial sites in NC matrices. The Ni:W:C ratios in the precursors have been fine-tuned, resulting in an optimized HER catalyst with low overpotential and high stability (21 mV at 10 mA·cm⁻² for 60 h in 1.0 M KOH). The critical role of NiSe/WSe₂ interfacial sites in the H₂O adsorption/dissociation and H₂ evolution process of the HER has been revealed by XAS and DFT calculations. This work offers an effective strategy for constructing well-defined heterostructures with enriched active sites and provides an in-depth understanding of the HER mechanism over the dual active centers on the heterointerface. Furthermore, given the unlimited tunability of both MOFs and POMs, this ambiphilic PDA bridging strategy is expected to open the way to the rational design of heterometallic electrocatalysts by engineering interfacial active sites for

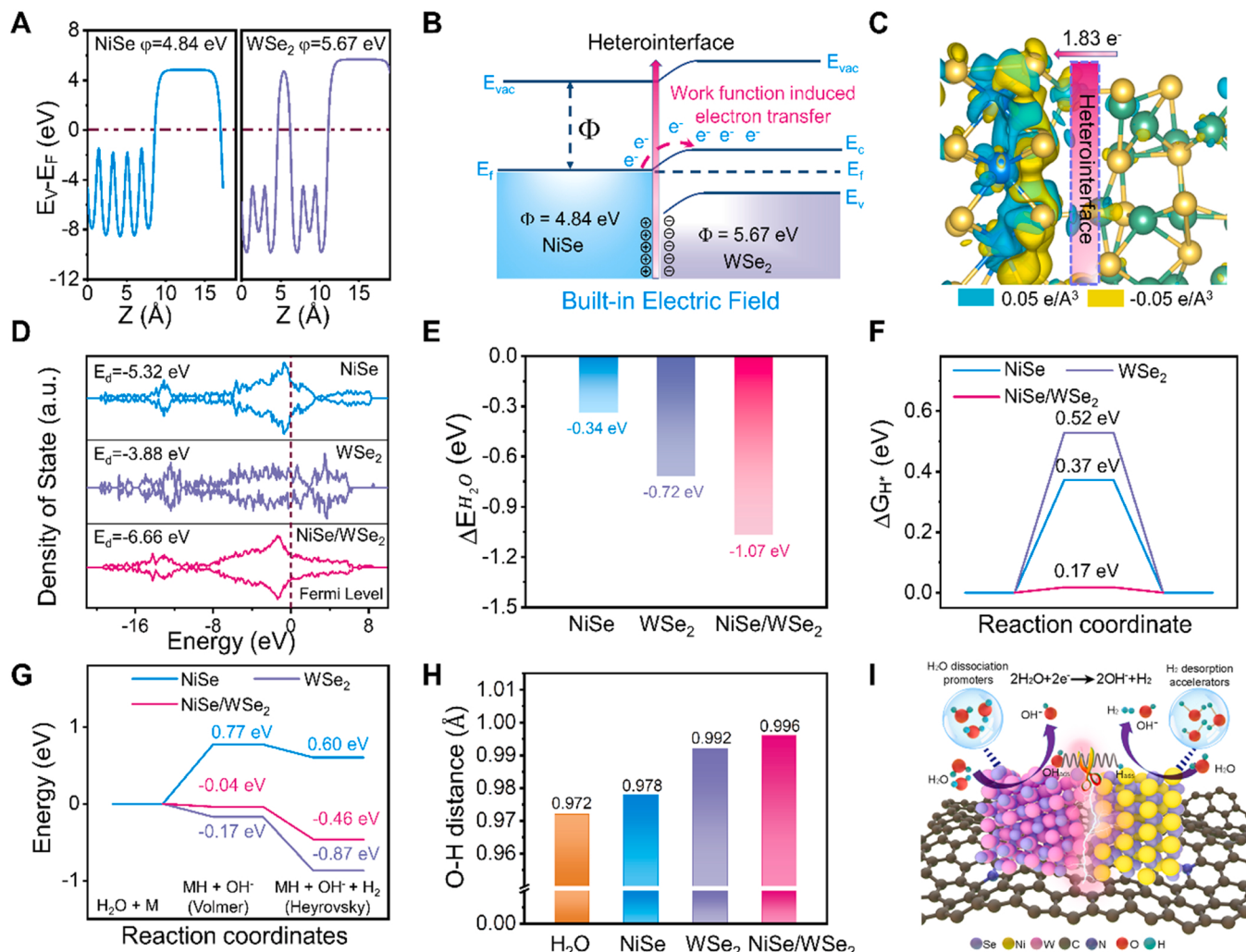


Fig. 5. (A) Electrostatic potential profiles of NiSe (101) and WSe₂ (002) surfaces, and both profiles are plotted relative to the corresponding Fermi levels. (B) Schematic energy band diagrams of the NiSe/WSe₂ heterostructure. The corresponding Fermi level (E_F), work function (Φ), vacuum level (E_{vac}), valence band (E_v) and conduction band (E_c) are shown. (C) The difference charge density in NiSe/WSe₂ heterojunctions. (D) The density of states (DOS) of WSe₂, NiSe, and NiSe/WSe₂, with the Fermi level was set at 0 eV. (E) The H₂O adsorption free energy of NiSe, WSe₂, and NiSe/WSe₂. (F) The H adsorption free energy of NiSe, WSe₂, and NiSe/WSe₂. (G) The calculated free-energy diagram of HER under alkaline conditions of NiSe, WSe₂, and NiSe/WSe₂. (H) The O-H bond distance in the H₂O molecule before and after H₂O binding on NiSe, WSe₂, and NiSe/WSe₂. (I) The proposed alkaline HER mechanism for NiSe/WSe₂ heterojunctions.

energy conversion applications.

CRediT authorship contribution statement

Zhaodi Huang and Shuai Yuan conceived the original idea, analysed the data, and co-wrote the paper. Zhaodi Huang and Youcong Li carried out the synthesis and electrochemical measurements. Chao Feng, Shoufu Cao, Yucang Liang and Xunli Li helped with the DFT calculations, XAS measurements and partial data analysis. Daofeng Sun, Fangna Dai and Bu Xu wrote the manuscript and discussed the results. Special thanks to Professor Cai Bin from Shandong University for his help in discussing the results. The other authors discussed the results and commented on the manuscript.

Declaration of Competing Interest

The authors declare that they have no known competing financial interests or personal relationships that could have appeared to influence the work reported in this paper.

Data availability

Data will be made available on request.

Acknowledgements

This work was supported by the National Natural Science Foundation of China (Grant Nos. 21875285, 22275210, 22271141), Natural Science Foundation of Jiangsu Province (BK20220765), Shandong Natural Science Fund (ZR2020KB010), Key Research and Development Projects of Shandong Province (2019JZZY010331), the Fundamental Research Funds for the Central Universities (19CX05001A), and the Outstanding Youth Science Fund Projects of Shandong Province (2022HWYQ-070).

Appendix A. Supporting information

Supplementary data associated with this article can be found in the online version at doi:10.1016/j.apcatb.2023.122769.

References

[1] M.S. Dresselhaus, I.I. Thomas, *Nature* 414 (2001) 6.

[2] X. Wang, W. Zhou, Y. Wang, L. Gong, X. Liu, X. Zhou, *Nano Energy* 109 (2023), 108253.

[3] Y. Zheng, Y. Jiao, A. Vasileff, S. Qiao, *Angew. Chem. Int. Ed.* 57 (2018) 7568–7579.

[4] G. Cai, W. Zhang, L. Jiao, S.-H. Yu, H.-L. Jiang, *Chem* 2 (2017) 791–802.

[5] Y. Yang, H. Yao, Z. Yu, S.M. Islam, H. He, M. Yuan, Y. Yue, K. Xu, W. Hao, G. Sun, H. Li, S. Ma, P. Zapol, M.G. Kanatzidis, *J. Am. Chem. Soc.* 141 (2019) 10417–10430.

[6] H. Li, S. Chen, Y. Zhang, Q. Zhang, X. Jia, Q. Zhang, L. Gu, X. Sun, L. Song, X. Wang, *Nat. Commun.* 9 (2018) 2452.

[7] Z. Chen, H. Qing, R. Wang, R. Wu, *Energy Environ. Sci.* 14 (2021) 3160–3173.

[8] J. Zhang, T. Wang, D. Pohl, B. Rellinghaus, R. Dong, S. Liu, X. Zhuang, X. Feng, *Angew. Chem. Int. Ed.* 55 (2016) 6702–6707.

[9] Y. Du, W. Weng, Z. Zhang, Y. He, J. Xu, T. Yang, J. Bao, X. Zhou, *Chin. J. Chem.* 39 (2021) 1878–1884.

[10] Y. Liu, Y. Chen, Y. Tian, T. Sakthivel, H. Liu, S. Guo, H. Zeng, Z. Dai, *Adv. Mater.* 34 (2022) 2203615.

[11] D.Y. Chung, J.M. Yoo, Y.-E. Sung, *Adv. Mater.* 30 (2018) 1704123.

[12] L. Zhang, K. Doyle-Davis, X. Sun, *Energy Environ. Sci.* 12 (2019) 492–517.

[13] H.-C. Zhou, J.R. Long, O.M. Yaghi, *Chem. Rev.* 112 (2012) 673–674.

[14] M. Zhao, K. Yuan, Y. Wang, G. Li, J. Guo, L. Gu, W. Hu, H. Zhao, Z. Tang, *Nature* 539 (2016) 76–80.

[15] H. Wang, Y. Jin, N. Sun, W. Zhang, J. Jiang, *Chem. Soc. Rev.* 50 (2021) 8874–8886.

[16] L. Lei, F. Chen, Y. Wu, J. Shen, X.-J. Wu, S. Wu, S. Yuan, *Sci. China Chem.* 65 (2022) 2205–2213.

[17] Z. Kou, W. Zang, Y. Ma, Z. Pan, S. Mu, X. Gao, B. Tang, M. Xiong, X. Zhao, A. K. Cheetham, L. Zheng, J. Wang, *Nano Energy* 67 (2020), 104288.

[18] C. Chen, A. Wu, H. Yan, Y. Xiao, C. Tian, H. Fu, *Chem. Sci.* 9 (2018) 4746–4755.

[19] Z.-H. Wang, X.-F. Wang, Z. Tan, X.-Z. Song, *Mater. Today Energy* 19 (2021), 100618.

[20] D.-L. Meng, C.-H. Chen, J.-D. Yi, Q. Wu, J. Liang, Y.-B. Huang, R. Cao, *Research* 2019 (2019) 1–12.

[21] L. Peng, S. Yang, S. Jawahery, S.M. Moosavi, A.J. Huckaba, M. Asgari, E. Oveisi, M. K. Nazeeruddin, B. Smit, W.L. Queen, *J. Am. Chem. Soc.* 141 (2019) 12397–12405.

[22] D.T. Sun, L. Peng, W.S. Reeder, S.M. Moosavi, D. Tiana, D.K. Britt, E. Oveisi, W. L. Queen, *ACS Cent. Sci.* 4 (2018) 349–356.

[23] J. Liebscher, R. Mrówczyński, H.A. Scheidt, C. Filip, N.D. Hădăde, R. Turcu, A. Bende, S. Beck, *Langmuir* 29 (2013) 10539–10548.

[24] S. Yang, L. Peng, D.T. Sun, M. Asgari, E. Oveisi, O. Trukhina, S. Bulut, A. Jamali, W. L. Queen, *Chem. Sci.* 10 (2019) 4542–4549.

[25] S.R. Caskey, A.G. Wong-Foy, A.J. Matzger, *J. Am. Chem. Soc.* 130 (2008) 10870–10871.

[26] Z. Wang, Y. Zou, Y. Li, Y. Cheng, *Small* 16 (2020) 1907042.

[27] W. Zhang, X. Chen, H. Xu, Y. Liu, X. Zhao, Z. Zhang, L. Li, Chin, *J. Chem.* 40 (2022) 1585–1591.

[28] L. Ye, Y. Ying, D. Sun, Z. Zhang, L. Fei, Z. Wen, J. Qiao, H. Huang, *Angew. Chem. Int. Ed.* 59 (2020) 3244–3251.

[29] N. Yao, R. Meng, F. Wu, Z. Fan, G. Cheng, W. Luo, *Appl. Catal. B Environ.* 277 (2020), 119282.

[30] X. Li, Y. Wang, J. Wang, Y. Da, J. Zhang, L. Li, C. Zhong, Y. Deng, X. Han, W. Hu, *Adv. Mater.* 32 (2020) 2003414.

[31] Y. Wang, X. Li, M. Zhang, J. Zhang, Z. Chen, X. Zheng, Z. Tian, N. Zhao, X. Han, K. Zaghib, Y. Wang, Y. Deng, W. Hu, *Adv. Mater.* 34 (2022) 2107053.

[32] Y. Men, S. Jia, P. Li, Y. Tan, J. Wang, P. Zhao, G. Cheng, S. Chen, W. Luo, *Chem. Eng. J.* 433 (2022), 133831.

[33] G. Zhang, A. Wang, L. Niu, W. Gao, W. Hu, Z. Liu, R. Wang, J. Chen, *Adv. Energy Mater.* 12 (2022) 2103511.

[34] K. Wang, Y. Guo, Z. Chen, D. Wu, S. Zhang, B. Yang, J. Zhang, *InfoMat* 4 (2022).

[35] Y. Li, X. Tan, H. Tan, H. Ren, S. Chen, W. Yang, S.C. Smith, C. Zhao, *Energy Environ. Sci.* 13 (2020) 1799–1807.

[36] R. Li, Y. Li, P. Yang, P. Ren, D. Wang, X. Lu, R. Xu, Y. Li, J. Xue, J. Zhang, M. An, J. Ma, B. Wang, H. Liu, S. Dou, *Appl. Catal. B Environ.* 318 (2022), 121834.

[37] Y. Liu, X. Luo, C. Zhou, S. Du, D. Zhen, B. Chen, J. Li, Q. Wu, Y. Iru, D. Chen, *Appl. Catal. B Environ.* 260 (2020), 118197.

[38] Y. Gu, A. Wu, Y. Jiao, H. Zheng, X. Wang, Y. Xie, L. Wang, C. Tian, H. Fu, *Angew. Chem. Int. Ed.* 60 (2021) 6673–6681.

[39] J. Wu, R. Zhao, H. Xiang, C. Yang, W. Zhong, C. Zhang, Q. Zhang, X. Li, N. Yang, *Appl. Catal. B Environ.* 292 (2021), 120200.

[40] Y. Zhang, B. Ouyang, J. Xu, S. Chen, R.S. Rawat, H.J. Fan, *Adv. Energy Mater.* 6 (2016) 1600221.

[41] X. Luo, P. Ji, P. Wang, R. Cheng, D. Chen, C. Lin, J. Zhang, J. He, Z. Shi, N. Li, S. Xiao, S. Mu, *Adv. Energy Mater.* 10 (2020) 1903891.

[42] H. Jin, X. Liu, Y. Jiao, A. Vasileff, Y. Zheng, S.-Z. Qiao, *Nano Energy* 53 (2018) 690–697.

[43] J. Zhang, T. Wang, D. Pohl, B. Rellinghaus, R. Dong, S. Liu, X. Zhuang, X. Feng, *Angew. Chem. Int. Ed.* 55 (2016) 6702–6707.

[44] H. Zhou, F. Yu, Q. Zhu, J. Sun, F. Qin, L. Yu, J. Bao, Y. Yu, S. Chen, Z. Ren, *Energy Environ. Sci.* 11 (2018) 2858–2864.

[45] Q. Hong, Y. Wang, R. Wang, Z. Chen, H. Yang, K. Yu, Y. Liu, H. Huang, Z. Kang, P. W. Menezes, *Small* (2023) 2206723.

[46] K. Guo, Y. Wang, S. Yang, J. Huang, Z. Zou, H. Pan, P.S. Shinde, S. Pan, J. Huang, C. Xu, *Sci. Bull.* 66 (2021) 52–61.

[47] K. Guo, Y. Wang, J. Huang, H. Li, Y. Peng, C. Xu, *Chem. Eng. J.* 454 (2023), 140488.

[48] Q. Yu, X. Liu, G. Liu, X. Wang, Z. Li, B. Li, Z. Wu, L. Wang, *Adv. Funct. Mater.* 32 (2022) 2205767.

[49] L. Zhao, Y. Zhang, Z. Zhao, Q.-H. Zhang, L.-B. Huang, L. Gu, G. Lu, J.-S. Hu, L.-J. Wan, *Nat. Sci. Rev.* 7 (2020) 27–36.

[50] E. Prouzet, J. Heising, M.G. Kanatzidis, *Chem. Mater.* 15 (2003) 412–418.

[51] C. Feng, C. Chen, G. Xiong, D. Yang, Z. Wang, Y. Pan, Z. Fei, Y. Lu, Y. Liu, R. Zhang, X. Li, *Appl. Catal. B Environ.* 328 (2023), 122528.

[52] X. Wang, L. Zhao, X. Li, Y. Liu, Y. Wang, Q. Yao, J. Xie, Q. Xue, Z. Yan, X. Yuan, W. Xing, *Nat. Commun.* 13 (2022) 1596.